nature catalysis

Article

https://doi.org/10.1038/s41929-025-01450-2

Single-atom photocatalysis boosting oxidant-free cross-dehydrogenative couplings of (hetero)arenes with nucleophiles

Received: 7 June 2024

Accepted: 23 October 2025

Published online: 01 December 2025

Check for updates

Yang Shi[1,6], Xiao Hai[2,6], Lei Cheng[3,6], Haolin Du[1,4], Xiaoye Yu[1], Hwee Ting Ang[1], Jiale Wu[1], Jinxing Chen[1], Gan Wang[1], Jiong Lu[1,5] ✉ & Jie Wu[1,5] ✉

Cross-dehydrogenative coupling (CDC) reactions provide a facile approach for direct (hetero)aromatic C(sp^2)–C and C(sp^2)–heteroatom bond formation but conventionally rely on stoichiometric oxidants. Here we introduce single-platinum-atom-decorated graphitic carbon nitride (Pt-g-C_3N_4) as a recyclable heterogeneous photocatalyst for hydrogen-evolution CDC reactions between various (hetero)arenes and nucleophiles. Pt-g-C_3N_4 exhibits exceptional stability (10 cycles) with minimal platinum leaching (<0.02 ppm). Notably, the photocatalytic system showcases substantial utility and practicality in synthetic chemistry, enabling late-stage functionalization of pharmaceuticals and optoelectronic materials, and scalable (decagram) drug synthesis via a simple, in-house-built high-speed circulation flow system. Mechanistic investigations through control experiments and structural characterization elucidate the pivotal role of isolated platinum sites and substrate electronic properties in governing reaction selectivity. The integration of hydrogen-evolution CDC reactions with recyclable heterogeneous photocatalysis represents one of the greenest strategies for chemical synthesis, underscoring the promising future of single-atom catalysts as photocatalysts.

Functionalized (hetero)arenes are ubiquitous structural motifs in drug design due to their pivotal role in improving pharmacological activity and target specificity. Notable examples of drug molecules containing these motifs include timolol, a β-adrenergic-blocking agent[1], and piboserod, a 5-HT_4 serotonin receptor antagonist[2], among others[3–8] (Fig. 1a). Conventionally, the rapid construction of C(sp^2)–heteroatom and C(sp^2)–C bonds heavily relies on transition metal-catalysed cross-coupling reactions that utilize prefunctionalized (hetero)aryl halides with nucleophiles, such as Suzuki-type, Ullmann-type and Buchwald–Hartwig-type coupling reactions[9–11]. However, over the past two decades, cross-dehydrogenative coupling (CDC) reactions have emerged as a powerful alternative, enabling the direct cross-coupling without the need for prefunctionalization via halides or metallic reagents, thereby simplifying synthetic routes and enhancing overall reaction efficiency.

Efforts to construct (hetero)aromatic C(sp^2)–heteroatom and C(sp^2)–C bonds via CDC strategies have shown promising outcomes through diverse strategies, including transition metal catalysis[12–17], photocatalysis[18–24] and electrochemical synthesis[24–31] (Fig. 1b). However, in transition metal catalysis, the need of stoichiometric oxidants

A full list of affiliations appears at the end of the paper. ✉e-mail: chmluj@nus.edu.sg; chmjie@nus.edu.sg

https://doi.org/10.1038/s41929-025-01450-2

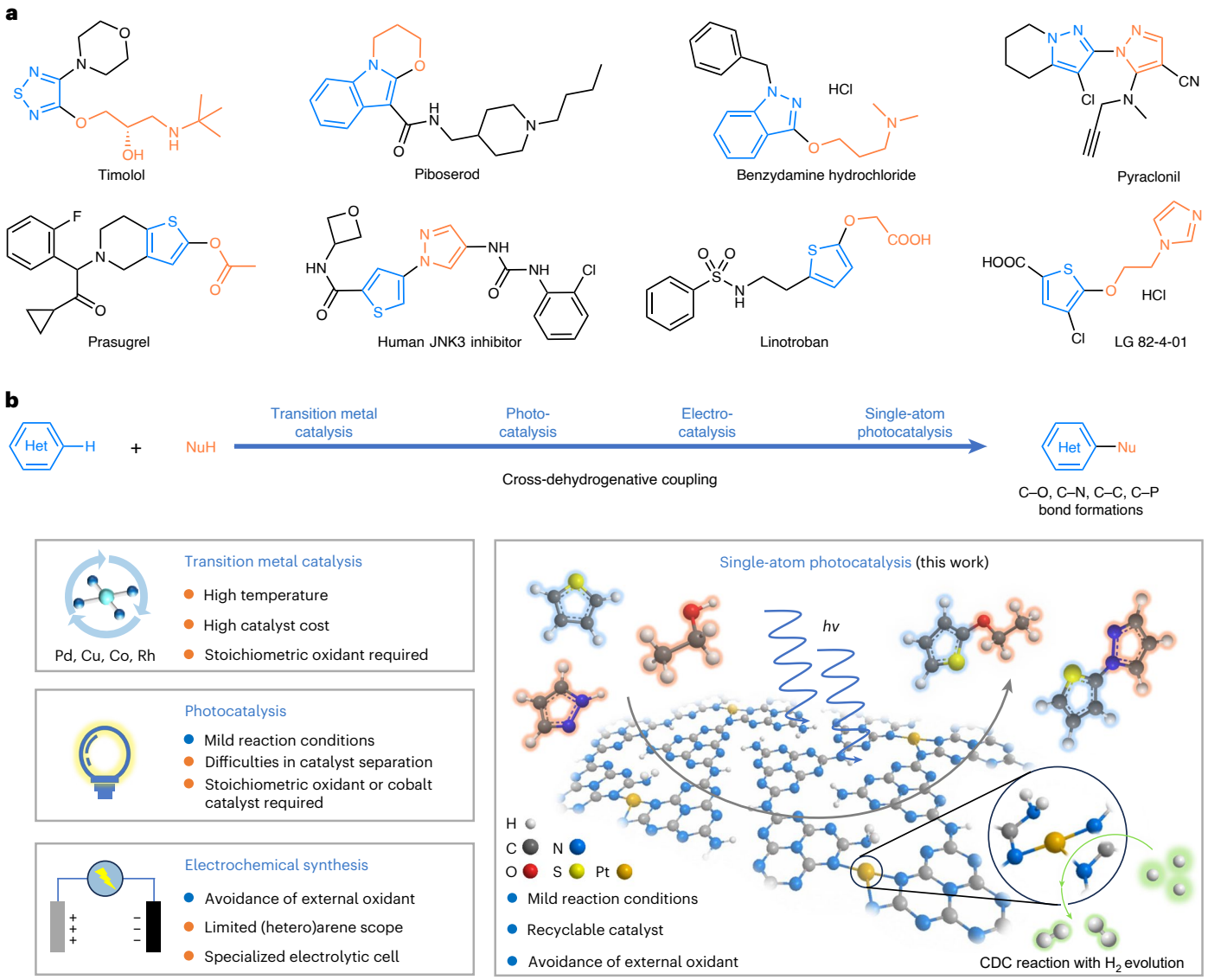

Fig. 1 | CDC reactions between (hetero)arenes and nucleophiles. a, Selected examples of drug molecules featuring (hetero)aromatic moieties. **b**, Previous strategies for the construction of (hetero)aromatic C(sp^2)–heteroatom and C(sp^2)–C bonds via CDC reactions and strategy for hydrogen-evolution CDC reactions via single-atom photocatalysis.

remains indispensable due to the oxidative nature of CDC reactions, leading to substantial waste especially when large quantities of metal salts and hypervalent iodine oxidants are used. Moreover, the inclusion of directing groups is frequently essential to achieve the desired selectivity, which prolongs the synthetic sequence. Additionally, harsh conditions such as elevated temperature and high catalyst loadings are often involved. Photocatalysis emerges as a compelling alternative, offering mild reaction conditions and excellent functional group compatibility in forging C(sp^2) bonds through CDC reactions, albeit still relying on stoichiometric oxidants in most cases. Notable exceptions, pioneered by the Wu[18] and Lei groups[22], have demonstrated effective hydrogen-evolution CDC reactions using a combination of cobalt oxime complexes and photocatalysts, obviating the need for external oxidants, even though more than 5 mol% cobalt oxime complexes are normally required. Electrochemical synthesis represents another strategy for hydrogen-evolution CDC reactions, with H_2 release at the cathode. However, this strategy often suffers from a limited scope of substrates and requires specialized electrolytic cell apparatus[32]. Consequently, the development of a convenient hydrogen-evolution CDC reaction with broad substrate adaptability, devoid of external oxidants and specialized electrochemical equipment, remains an important objective with profound scientific and practical implications.

Single-atom catalysts (SACs), composed of individual metal atoms uniformly dispersed and anchored onto a support material, offer a potential bridge between homogeneous and heterogeneous catalysis. Their optimal atomic utilization and tunable local coordination environment of active sites offer exceptional performance, cost reduction, and notable catalytic activity and selectivity. Furthermore, as heterogenous catalysts, SACs exhibit great stability and enable easy recovery and reuse, making them attractive for sustainable catalysis. Hence, the field of single-atom photocatalysis (SAPC), extensively explored in H_2 evolution and CO_2 reduction[33–35], is gaining prominence in organic synthesis even though it is still in its infancy. For instance, several single-nickel-atom-anchored carbon nitride (CN) photocatalysts have shown excellent performance in cross-coupling reactions involving C–X bonds with alcohols[36], amines[37] or carboxylic acids[38]. However, the application of SAPCs in general CDC reactions remains undeveloped. We envisioned that integrating SAPCs into hydrogen-evolution CDC reactions would yield numerous compelling advantages, including mild, oxidant-free conditions, low metal loading, and excellent catalyst stability and recyclability.

https://doi.org/10.1038/s41929-025-01450-2

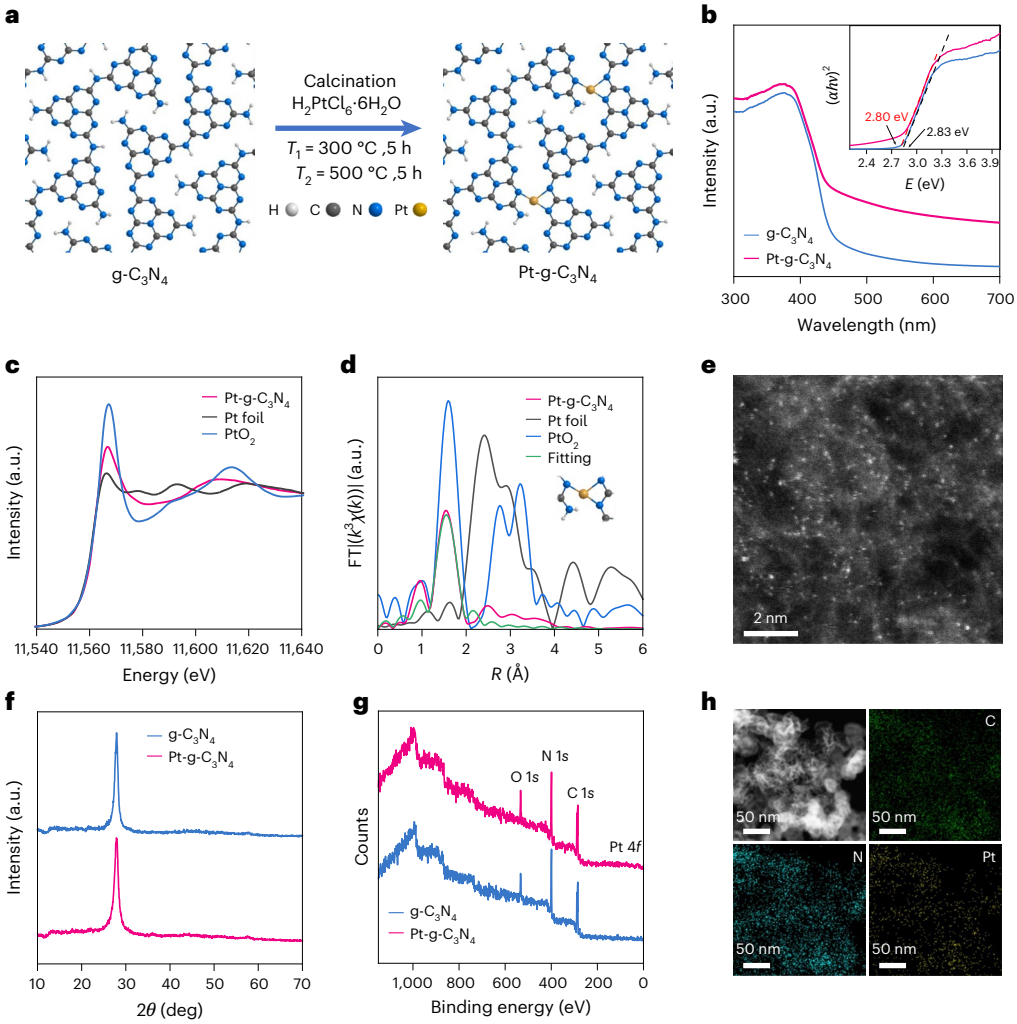

Fig. 2 | Synthesis and characterization of Pt-g-C_3N_4. **a**, Preparation of Pt-g-C_3N_4. **b**, UV–vis DRS spectra of g-C_3N_4 and Pt-g-C_3N_4. **c**, Platinum L_3-edge XANES spectra of Pt-g-C_3N_4, platinum foil and PtO_2 as the reference. **d**, k^3-weighted Fourier-transformed (FT) EXAFS spectra of Pt-g-C_3N_4, platinum foil and PtO_2 as the reference. **e**, ADF-STEM image of Pt-g-C_3N_4. **f**, XRD patterns of g-C_3N_4 and Pt-g-C_3N_4. **g**, Full-scan XPS spectra of g-C_3N_4 and Pt-g-C_3N_4. **h**, ADF-STEM image and corresponding elemental maps of Pt-g-C_3N_4.

In this study, we present the development of a highly efficient and robust photocatalytic hydrogen-evolution CDC reaction between diverse (hetero)arenes and nucleophiles, catalysed by single-platinum-atom-decorated graphitic carbon nitride (Pt-g-C_3N_4), delivering a series of (hetero)aromatic C(sp^2)–heteroatom and C(sp^2)–C bond formations (Fig. 1b). Notably, cross-couplings, such as thiophenes with alcohols, carbamates, disulfonimides and 1,3-dicarbonyl compounds, formidable challenges even in homogeneous systems, have been realized. By judiciously selecting the metal catalyst and optimizing the utilization of metal atoms, we achieved a low metal loading of 0.08 mol% Pt for effective couplings of a wide range of (hetero)arenes, alcohols, nitrogen-containing nucleophiles, 1,3-dicarbonyl compounds, diarylphosphine oxides and carboxylic acids. The practicality and synthetic application of this heterogeneous photocatalytic platform were demonstrated by comparative experiments with homogeneous systems, recyclability tests, late-stage functionalization of various pharmaceuticals and optoelectronic materials, and by streamlined synthesis of drug molecules assisted by a simple in-house-built high-speed circulation flow (HSCF) system[39].

Results

Design, synthesis and characterization of SACs

Initially, SACs were meticulously designed based on several critical considerations: selecting a supporting material with an abundance of surface trapping sites for single metal atoms, a high surface area, visible-light absorption and appropriate redox potential under photoexcitation; choosing a metal with optimal performance in H_2 evolution; and ensuring ease of preparation and cost effectiveness. Among various semiconducting support materials, g-C_3N_4 emerged as an ideal choice due to its well-acknowledged efficiency in artificial photocatalytic hydrogen evolution and its extensive applications in photoredox catalytic organic synthesis[40,41]. The ample presence of nitrogen atoms provides sufficient anchoring sites for single atoms, while its band structure ensures adequate photoredox capability[42], unequivocally meeting the criteria for supporting materials. Additionally, g-C_3N_4 is easily prepared from inexpensive materials with a well-documented synthesis procedure, making it a cost-effective option[42]. Among numerous noble metals, platinum exhibits the lowest activation energy for the catalytic reduction of protons to hydrogen and has demonstrated outstanding efficiency in photocatalytic water splitting[43,44]. Notably, the integration of a single-atom co-catalyst could not only facilitate efficient H_2 evolution but also address the prevalent issues of fast recombination of photogenerated electron–hole pairs of g-C_3N_4. Consequently, the Pt-g-C_3N_4 SAC was selected for further exploration in photocatalytic hydrogen-evolution CDC reactions.

The Pt-g-C_3N_4 SAC was synthesized on a 5-g scale using a well-documented two-step annealing method[45], involving the precise

https://doi.org/10.1038/s41929-025-01450-2

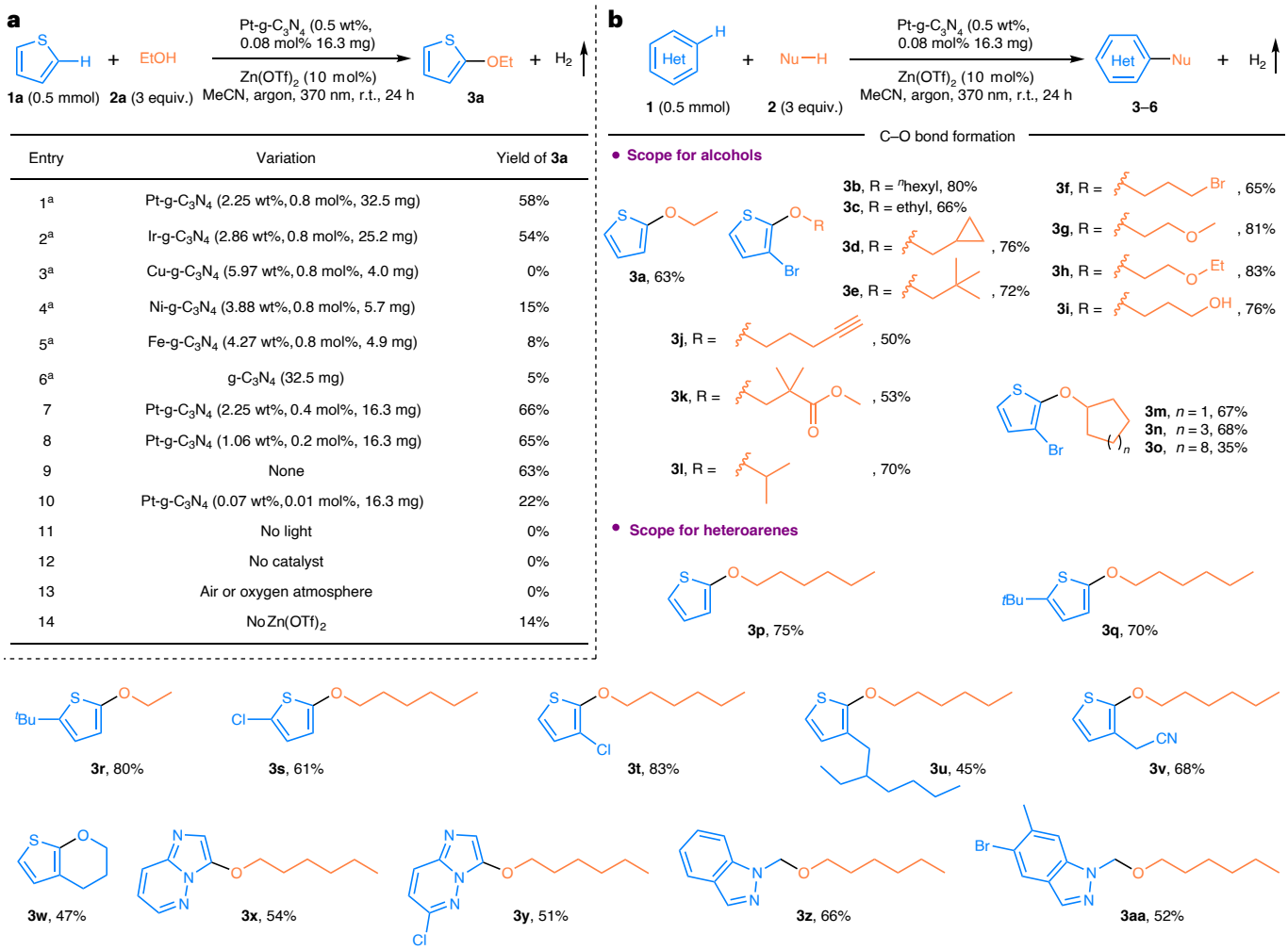

Entry	Variation	Yield of **3a**
1[a]	Pt-g-C_3N_4 (2.25 wt%, 0.8 mol%, 32.5 mg)	58%
2[a]	Ir-g-C_3N_4 (2.86 wt%, 0.8 mol%, 25.2 mg)	54%
3[a]	Cu-g-C_3N_4 (5.97 wt%, 0.8 mol%, 4.0 mg)	0%
4[a]	Ni-g-C_3N_4 (3.88 wt%, 0.8 mol%, 5.7 mg)	15%
5[a]	Fe-g-C_3N_4 (4.27 wt%, 0.8 mol%, 4.9 mg)	8%
6[a]	g-C_3N_4 (32.5 mg)	5%
7	Pt-g-C_3N_4 (2.25 wt%, 0.4 mol%, 16.3 mg)	66%
8	Pt-g-C_3N_4 (1.06 wt%, 0.2 mol%, 16.3 mg)	65%
9	None	63%
10	Pt-g-C_3N_4 (0.07 wt%, 0.01 mol%, 16.3 mg)	22%
11	No light	0%
12	No catalyst	0%
13	Air or oxygen atmosphere	0%
14	No $Zn(OTf)_2$	14%

Fig. 3 | Catalytic performance in hydrogen-evolution CDC reactions. **a**, Optimization of reaction conditions. [a]Reactions were carried out with 440-nm light irradiation at 50 °C. **b**, Substrate scope for (hetero)arenes and alcohols. Reaction conditions: (hetero)arene (0.5 mmol), alcohol (3 equiv.), Pt-g-C_3N_4 (0.5 wt%, 0.08 mol%, 16.3 mg), $Zn(OTf)_2$ (10 mol%, 18.2 mg), anhydrous MeCN (0.5 ml) at room temperature under an argon atmosphere for 24 h with light irradiation at 370 nm.

attachment of the platinum precursor to the nitrogen-rich anchor site, followed by the stepwise removal of the ligand to form the final single-atom structure (Fig. 2a). Subsequently, comprehensive characterization was conducted to assess the structural and electronic properties of the synthesized Pt-g-C_3N_4. The platinum content was measured at 0.5 wt% using inductively coupled plasma optical emission spectroscopy (ICP-OES) analysis. Ultraviolet–visible (UV–vis) diffuse reflectance spectroscopy measurements revealed bandgaps of 2.83 eV for g-C_3N_4 and 2.80 eV for Pt-g-C_3N_4, respectively (Fig. 2b), as determined using the Tauc plot method. The minimal change in bandgap with platinum-atom incorporation confirms that the intrinsic electronic band structure of g-C_3N_4 is well preserved. In the platinum L_3-edge X-ray absorption near edge structure (XANES) spectra, the intensity of the white line for the platinum single atom falls between that of platinum foil and PtO_2, suggesting the cationic nature of platinum species in the g-C_3N_4 matrix (Fig. 2c). Further confirmation from the binding energy of platinum $4f_{7/2}$ in the Pt-g-C_3N_4 sample, as determined by X-ray photoelectron spectroscopy (XPS, Supplementary Fig. 5), indicates a valence state of approximately +2. The Fourier-transformed extended X-ray absorption fine structure (EXAFS) spectrum of Pt-g-C_3N_4 shows a distinct peak at 1.5 Å, representing the first shell interatomic distances between platinum and nitrogen atoms, which is also supported by the fitting result (Fig. 2d, Supplementary Fig. 6 and Supplementary Table 3). The absence of any Pt–Pt peaks in the spectrum suggests that platinum is incorporated into g-C_3N_4 exclusively as isolated single atoms, with no tendency towards aggregation or crystallization. Consistently, the bright dots, corresponding to single metal atom sites, were captured in the annular dark-field scanning transmission electron microscopy (ADF-STEM) image, with no evidence of nanoparticles or clusters observed (Fig. 2e). In addition, the powder X-ray diffraction (XRD, Fig. 2f), XPS (Fig. 2g) and elemental mapping by energy dispersive X-ray spectroscopy (Fig. 2h) further verify the uniform dispersion of the platinum species in Pt-g-C_3N_4 across the entire area. Consequently, these detailed characterizations provide substantial evidence that the incorporation of platinum single atoms into the g-C_3N_4 framework was successful, while still preserving the integrity of the framework's inherent atomic and electronic structures.

Investigation of the performance of photocatalytic hydrogen-evolution cross-coupling reactions

The photocatalytic hydrogen-evolution CDC reaction with (hetero) arenes and nucleophiles was explored utilizing thiophene (**1a**) and ethanol (**2a**) as model substrates. To validate our SAC design, we initially investigated the reaction using SACs with various metallic atoms. Encouragingly, Pt-g-C_3N_4 resulted in a 58% yield of the desired product **3a** (Fig. 3a, entry 1), while other SACs, including iridium-,

https://doi.org/10.1038/s41929-025-01450-2

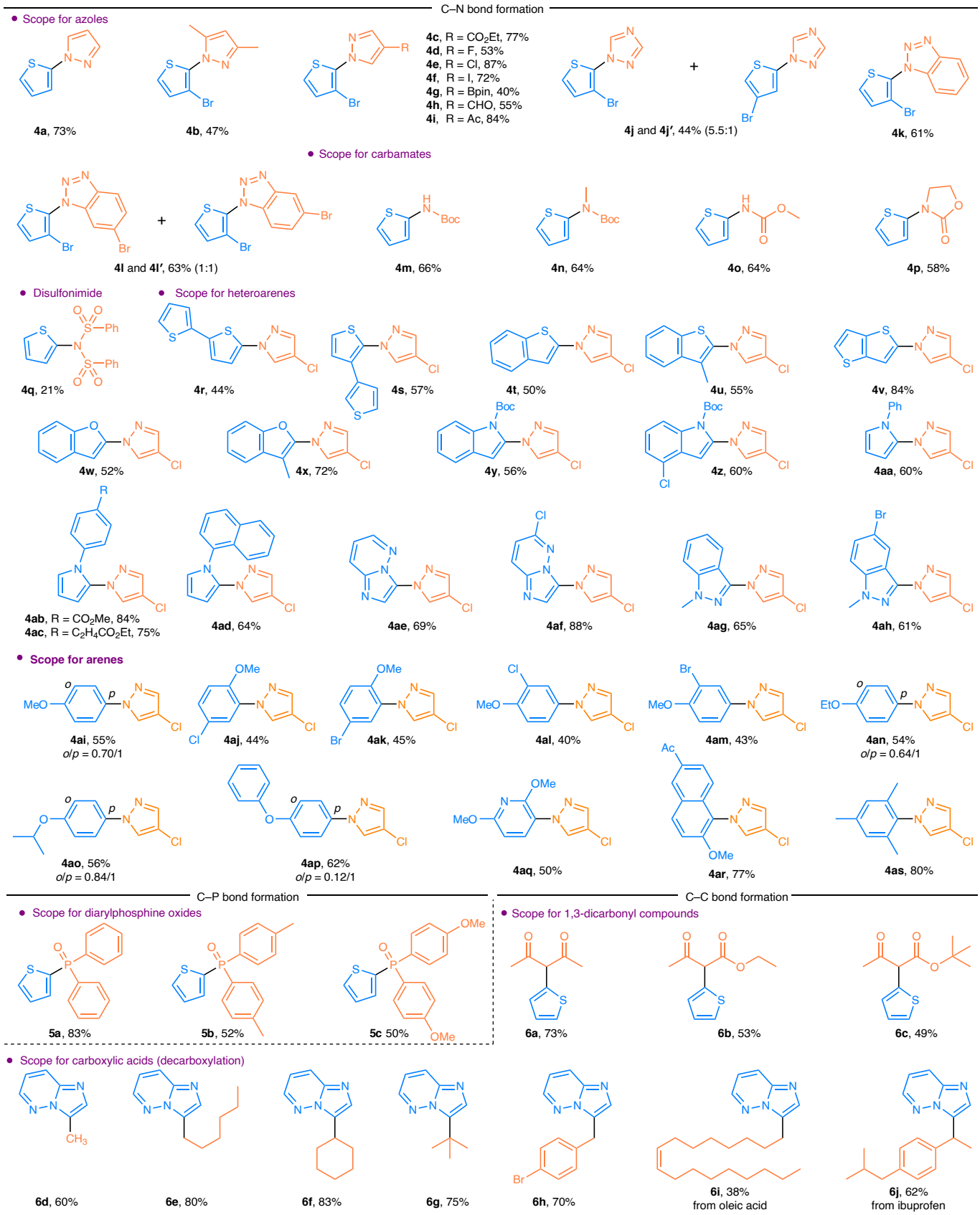

Fig. 4 | Substrate scope for (hetero)arenes and nucleophiles. Reaction conditions: (hetero)arene (0.5 mmol), nucleophile (3 equiv.), Pt-g-C_3N_4 (0.5 wt.%, 0.08 mol%, 16.3 mg), $Zn(OTf)_2$ (10 mol%, 18.2 mg), anhydrous MeCN (0.5 ml) at room temperature under an argon atmosphere for 24 h with light irradiation at 370 nm.

copper-, nickel- and iron-doped g-C_3N_4 showed substantial variations in catalytic efficiency (entries 2–5). g-C_3N_4 as a photocatalyst resulted in only 5% yield of **3a** (entry 6), indicating notable recombination of photogenerated electron–hole pairs on the catalyst. Subsequent solvent screening identified MeCN as the optimal reaction medium (Supplementary Table 5), while evaluation of various light sources revealed that 370-nm irradiation delivered the highest reaction efficiency (Supplementary Table 6). The maximized metal dispersion and atomic utilization efficiency of SACs allowed for a reduction in metal loading without compromising catalytic performance. Progressively decreasing the metal loading from 2.25 wt% to 0.5 wt% led to a negligible 5% decrease in yield; however, further reduction to 0.07 wt% markedly diminished the yield (Fig. 3a, entries 7–10). Considering both efficiency and cost, Pt-g-C_3N_4 at 0.5 wt% was identified as the optimal catalyst, with the detection of H_2 generation under these optimal conditions (Supplementary Fig. 7). Additional control experiments underscored the necessity of light, photocatalyst and an argon atmosphere (Fig. 3a, entries 11–13), while the absence of additive $Zn(OTf)_2$ led to considerably reduced yield (entry 14). The possibility of $Zn(OTf)_2$ acting as a Lewis acid and influencing the oxidation potential of **1a** was ruled out through cyclic voltammetry (CV) measurement (Supplementary Fig. 11). Further screening of various additives, with different combination of anions and cations, indicated that counteranions with low nucleophilicity were beneficial for this reaction (Supplementary Table 8), probably due to their involvement in stabilizing the transient thienyl radical cation intermediate[46,47]. Additional photocurrent measurements reveal that the introduction of $Zn(OTf)_2$ enhances the photocurrent density of Pt-g-C_3N_4 (Supplementary Fig. 18). Based on this observation, we propose that $Zn(OTf)_2$ functions as a buffering agent, interacting with photogenerated holes to suppress electron–hole recombination, thereby improving catalytic efficiency.

With the optimized conditions in hand, we subsequently investigated the scope of the reaction (Fig. 3b). Various primary alcohols with diverse functional groups, including alkyl chains, cyclic rings, halogens, alkoxy, free hydroxyl, alkynyl and ester groups, smoothly underwent regioselective CDC reaction with 3-bromothiophene, yielding thienyl alkyl ether products (**3b**–**3k**) with moderate to good yields. Notably, 1,3-propanediol exclusively produced mono C(sp^2)–O bond formation (**3i**) without any diether formation. Both acyclic (**3l**) and cyclic secondary alcohols ranging from 5-membered to 12-membered rings (**3m**–**3o**) also proved to be suitable nucleophiles. Regarding the scope of (hetero) arenes, thiophenes with various substituents at different positions were compatible with this photocatalytic system, delivering cross-coupling products (**3p**–**3v**) in satisfactory yields. Importantly, these reactions exhibited high regioselectivity, which corroborates with the formation of the most stable radical adducts between thiophene radical cations and alcohols. In addition, intramolecular C(sp^2)–O bond formation was evaluated using 3-(3-thienyl)-1-propanol, which gave cyclization product **3w** in 47% yield. Furthermore, nitrogen-containing heterocycles such as imidazo[1,2-*b*]pyridazines displayed high reactivity, with the CDC reaction occurring regioselectively at the C3 position (**3x**, **3y**). Interestingly, using 1-methylindazoles led to a switch in regioselectivity to α-N C(sp^3)–H couplings instead of C(sp^2)–O cross-couplings (**3z**–**3aa**).

Subsequent exploration involving various nucleophiles (Fig. 4) revealed pyrazole to be a remarkably efficient N–H partner in the CDC reaction. Investigation into different substituents on pyrazole, such as alkyl, ester, halogen, boronate, aldehyde and acetyl, demonstrated excellent compatibility (**4a**–**4i**), thereby enabling further product derivatization. Reaction with 1,2,4-triazole resulted in a mixture of regioisomers **4j** and **4j′** in a 5.5:1 ratio and moderate yield. Benzotriazoles were also well tolerated, yielding the corresponding amination products (**4k**, **4l**), where isomers (**4l**, **4l′**) derived from benzotriazole tautomers were obtained in a 1:1 ratio. To broaden the synthetic utility of C(sp^2)–N coupling, we explored additional nitrogen-containing nucleophiles beyond pyrazoles. Notably, carbamates (**4m**–**4p**) and disulfonimides (**4q**) effectively extended the substrate scope to include alkylamines, thus enabling two additional types of cross-coupling transformations for the synthesis of nitrogen-functionalized heteroarenes. Notably, the scope of (hetero)arenes displayed enhanced diversity in C(sp^2)–N coupling reactions compared with the C(sp^2)–O coupling reactions. Besides thiophenes (**4r**, **4s**), (hetero)arenes such as benzothiophenes (**4t**, **4u**), thienothiphenes (**4v**), benzofurans (**4w**, **4x**), indoles (**4y**, **4z**), and pyrroles (**4aa**–**4ad**), previously unreactive in C(sp^2)–O couplings, successfully underwent C(sp^2)–N couplings with 4-chloropyrazole. Imidazo[1,2-*b*]pyridazines (**4ae**, **4af**) and 1-methylindazoles (**4ag**, **4ah**) also effectively participated in the CDC reactions. Notably, 1-methylindazole substrate exhibited distinct regioselectivity compared to alkoxylation reactions (**4ag**, **4ah** versus **3z**, **3aa**), which can be attributed to the substantial difference in nucleophilicity between alcohols and pyrazoles. In addition to five-member ring systems, electron-rich six-member ring systems, including anisole derivatives (**4ai**–**4am**), phenyl ethers (**4an**–**4ap**), 2,6-dimethoxypyridine (**4aq**), naphthyl methyl ether (**4ar**) and mesitylene (**4as**), were also suitable substrates in our heterogeneous photocatalytic system.

Moreover, the synthetic utility of this protocol was further extended to C(sp^2)–P bond formation using diarylphosphine oxides as nucleophiles (**5a**–**5c**). Additionally, 1,3-dicarbonyl compounds served as effective nucleophiles in a C(sp^2)–C(sp^3) bond-forming transformation (**6a**–**6c**). Notably, using carboxylic acids as nucleophiles enabled a decarboxylative alkylation with imidazo[1,2-*b*]pyridazine, affording coupling products (**6d**–**6j**) in high yields. This represents a highly efficient and green Minisci-type transformation without the need of an external oxidant.

Synthetic applications

To explore the difference between our heterogeneous SAPC system and the homogeneous system, we compared the reaction efficiency of a commonly used homogeneous photocatalytic system[22] for hydrogen-evolution CDC reactions between (hetero)arenes and nucleophiles. As illustrated in Fig. 5a, the use of acridinium salt as the photocatalyst, in conjunction with the cobalt complex [$Co(dmgH)_2Cl_2$] as the hydrogen-evolution catalyst, led to dramatically reduced yields for products **3p**, **3z**, **4z**, **4aa** and **4ah**, while only moderate yields were achieved for products **4x** and **4af**. Additionally, when 3-bromothiophene (**1b**) was subjected to the homogeneous photocatalytic conditions, a mixture of product **3b** and debrominated **3p** was obtained in 12% yield. These experiments highlight the effectiveness and advance of our SAPC system for CDC reactions between (hetero) arenes and nucleophiles over homogeneous systems. Notably, the addition of $Zn(OTf)_2$ under these homogeneous conditions also gave improved yields (**4x** and **4af**), further supporting the role of $Zn(OTf)_2$ in stabilizing the transient thienyl radical cation intermediates.

One of the key advantages of heterogeneous catalysis is the ability to recycle and reuse the catalyst. Therefore, the recyclability of Pt-g-C_3N_4 in the photocatalytic hydrogen-evolution CDC reaction was examined. After the reaction, the Pt-g-C_3N_4 catalyst was effectively recycled through a straightforward process involving centrifugation, washing and drying steps, while maintaining its high catalytic activity over the course of 10 cycles (Fig. 5c). Negligible metal leaching into the solution (<0.02 ppm) was detected, with only a marginal reduction in metal loading observed after 10 cycles, decreasing from 0.5 wt% to 0.48 wt% as confirmed by ICP-OES analysis (Fig. 5b). The XRD spectra obtained before and after 10 cycles also showed no sign of metal aggregation in the catalyst (Fig. 5d). Additional characterizations, including XANES and EXAFS spectra of the recovered Pt-g-C_3N_4 (Fig. 5e,f), showed excellent overlap with those of the freshly prepared sample, with K_2PtCl_4 as a reference. These results suggested that the platinum valence state and coordination environment remain unchanged after recycling. Furthermore, the bright dots observed in the ADF-STEM image of the recovered Pt-g-C_3N_4 (Fig. 5g) clearly highlight the durability of

https://doi.org/10.1038/s41929-025-01450-2

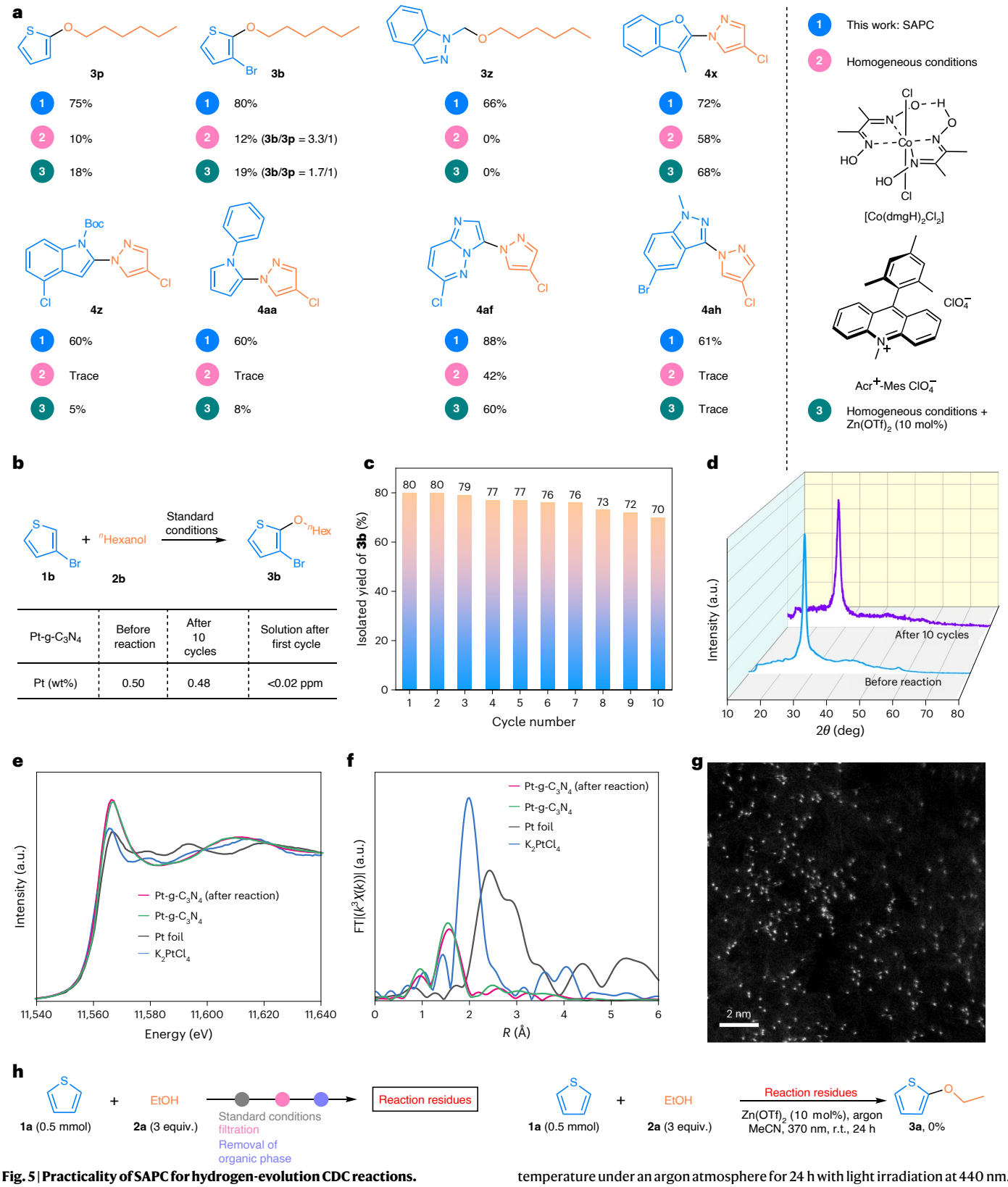

Fig. 5 | Practicality of SAPC for hydrogen-evolution CDC reactions. **a**, Comparison between homogeneous and single-atom heterogeneous photocatalytic conditions. Condition 1: standard conditions. Condition 2: (hetero)arene (0.3 mmol), nucleophile (4 equiv.), Acr^+-Mes ClO_4^- (7 mol%, 8.6 mg), $[Co(dmgH)_2Cl_2]$ (8 mol%, 8.7 mg), anhydrous MeCN (5.0 ml) at room temperature under an argon atmosphere for 24 h with light irradiation at 440 nm. Condition 3: condition 2 with $Zn(OTf)_2$ (10 mol%, 10.9 mg). **b**, Metal leaching test. **c**, Recycling test results. **d**–**g**, XRD pattern (**d**), platinum L_3-edge XANES (**e**), FT EXAFS spectra (**f**) and ADF-STEM image (**g**) of recovered Pt-g-C_3N_4. **h**, Reactivity study of the leached platinum.

https://doi.org/10.1038/s41929-025-01450-2

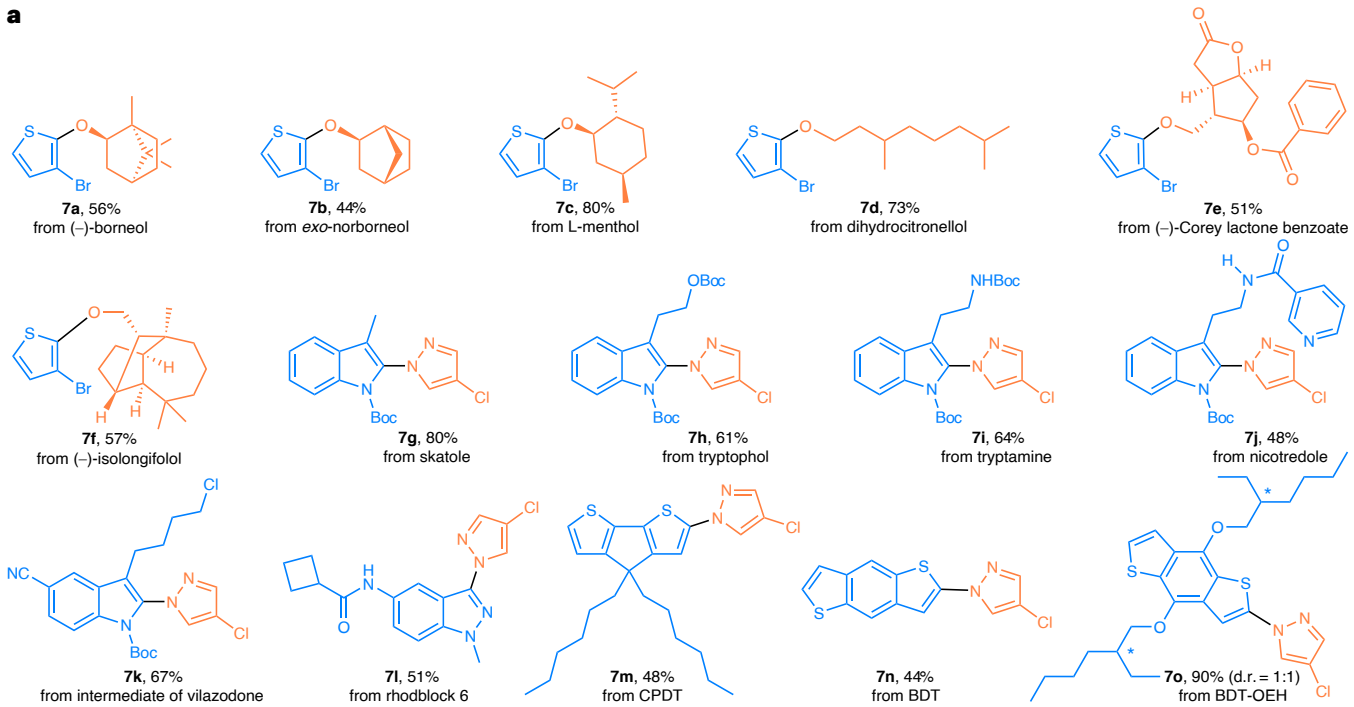

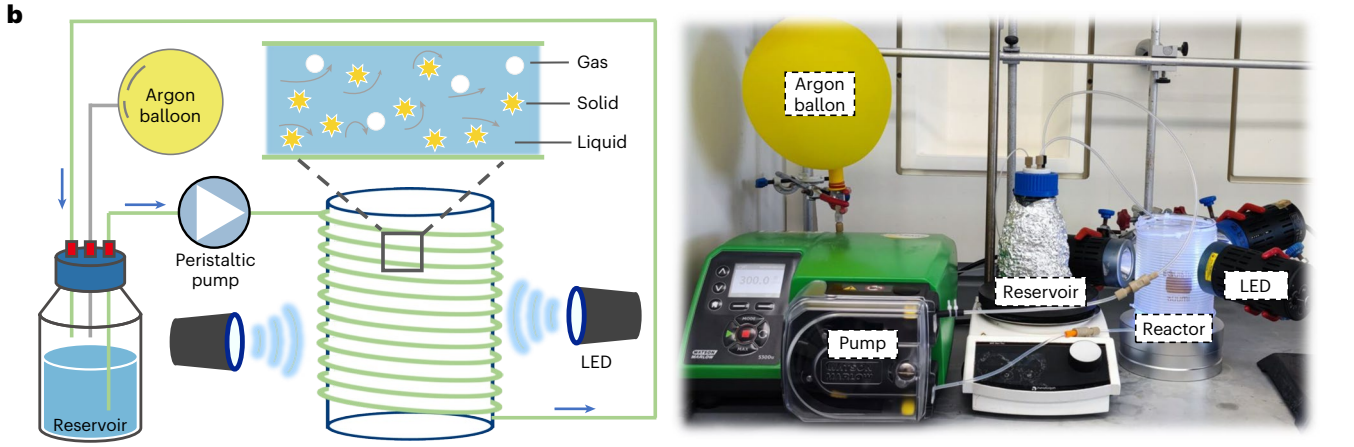

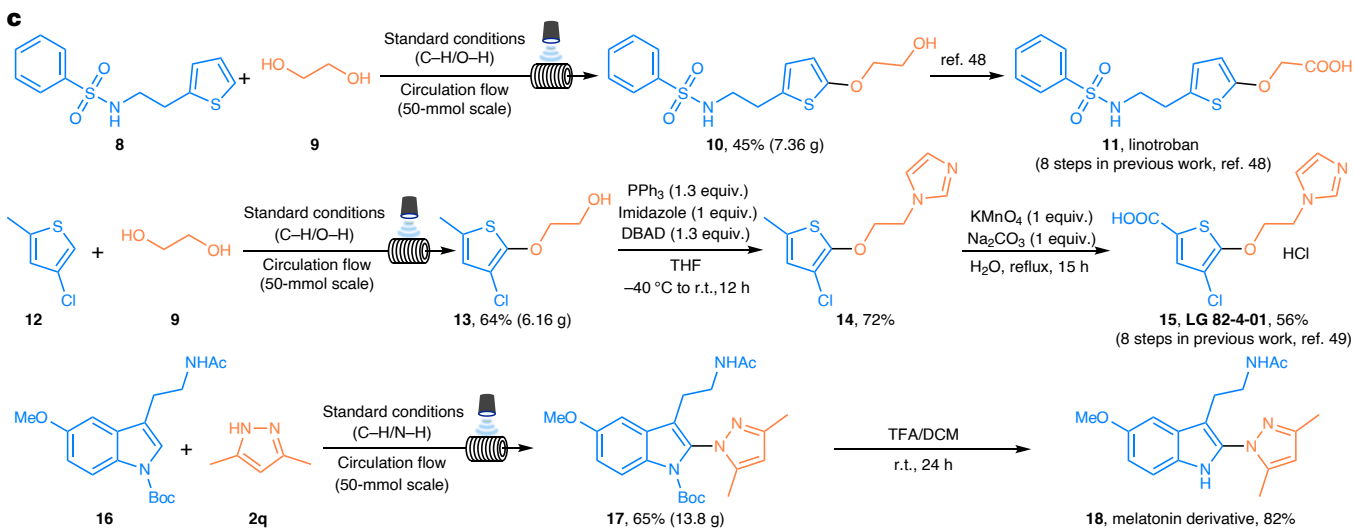

Fig. 6 | Synthetic applications. a, Late-stage modification of natural products, drugs and optoelectronic materials. Reaction conditions: standard conditions. **b**, Schematic illustration of the high-speed circulation flow system and platform set-up. **c**, Facile synthesis of linotroban, LG 82-4-01, and the melatonin derivative assisted by the HSCF system.

https://doi.org/10.1038/s41929-025-01450-2

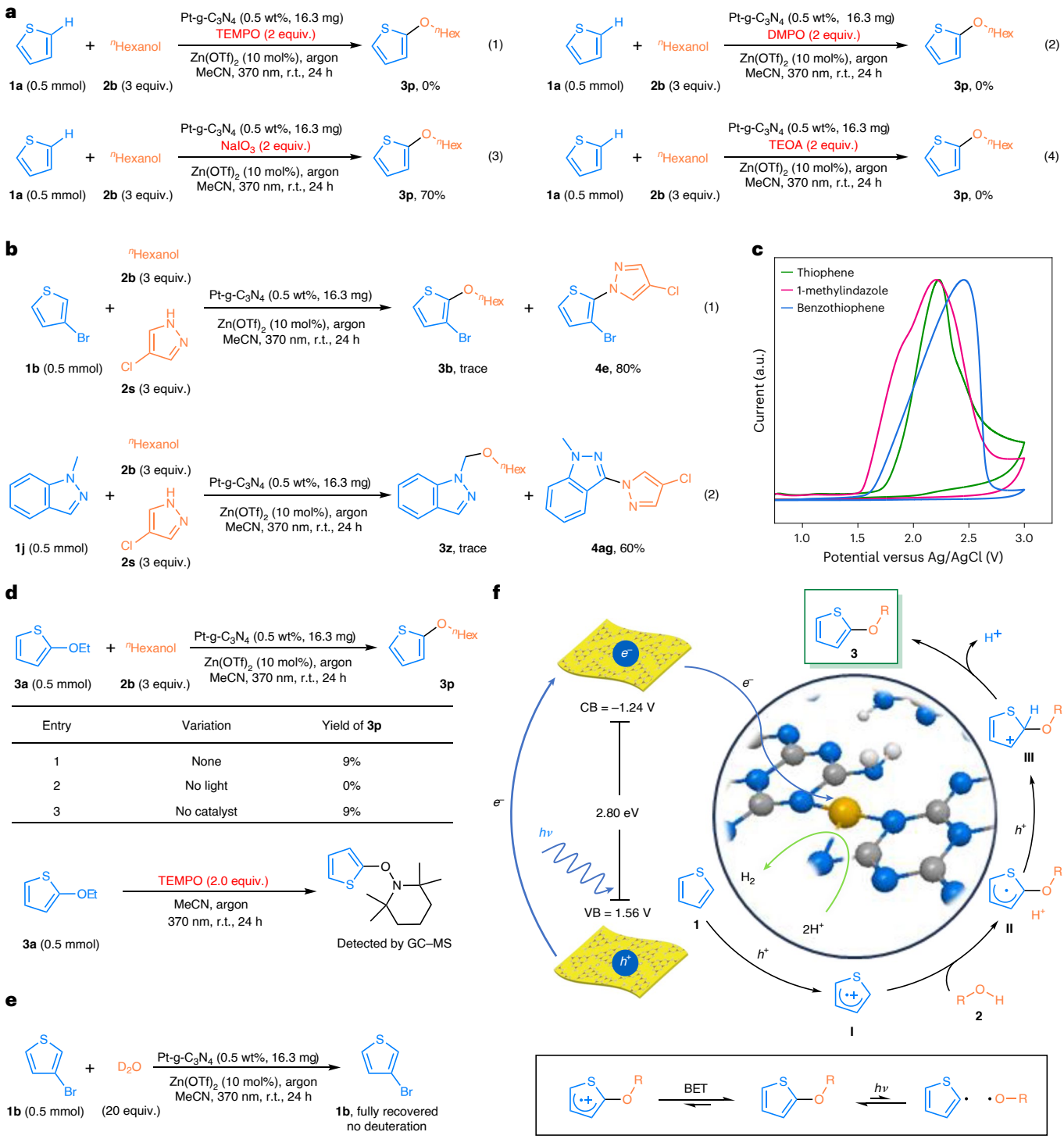

Fig. 7 | Control experiments for mechanistic studies. a, Control experiments. **b**, Intermolecular competition experiments. **c**, CV measurements for (hetero) aromatics. **d**, Functional group swapping and radical trapping experiments. GC–MS, gas chromatography–mass spectrometry. **e**, H/D exchange experiments. **f**, Proposed reaction mechanisms.

the catalyst, demonstrating its capability to be recycled and reused numerous times without notable loss of catalytic activity or structural integrity. Based on the experimental findings, we propose that the atomically dispersed platinum plays a dual role in enhancing both catalytic activity and stability. First, maximized atomic efficiency: platinum-single-atom active sites, existing as isolated metal atoms, theoretically offer 100% atomic utilization. In CDC reactions, these platinum atoms act as primary catalytic centres, directly participating in the coupling process and thereby avoiding the inefficiencies associated with the underutilization of bulk atoms typically observed in conventional nanoparticle catalysts. Second, dynamic stability: throughout the catalytic process, the single-atom platinum species remain firmly anchored on the g-C_3N_4 support, ensuring excellent recyclability and suppressing aggregation.

To exclude the possible catalytic activity from leached platinum, we conducted the model reaction using the reaction residues to replace Pt-g-C_3N_4 (Fig. 5h). The reaction residues were prepared via simple filtration and removal of the entire organic phase after the reaction.

No cross-coupling product **3a** was formed, confirming the absence of catalytic activity from any leached Pt.

Subsequently, our protocol was extended to late-stage functionalization across natural products, pharmaceuticals and optoelectronic materials (Fig. 6a). Diverse naturally occurring alcohols were subjected to the CDC reaction with 3-bromothiophene **1b**, delivering products (**7a**–**7f**) in moderate to good yields with excellent regioselectivity. Indole-based pharmaceutical compounds featuring a range of functionalities, proved amenable to C(sp^2)–N coupling (**7g**–**7k**). Additionally, *N*-methyl protected rhodblock 6, a Rho kinase inhibitor, reacted smoothly under the reaction conditions (**7l**). Beyond bioactive molecules, two prominent optoelectronic material frameworks, namely thiophene-based cyclopenta[2,1-*b*:3,4-*b*′]dithiophene (CPDT) and benzo[1,2-*b*:4,5-*b*′]dithiophene (BDT), were identified as suitable substrates, resulting in monoaminated products (**7m**–**7o**) in moderate to good yields.

Further demonstrating the practical applications of our strategy, a simple in-house-built high-speed circulation flow (HSCF) platform was utilized for the large-scale synthesis of pharmaceutical molecules (Fig. 6b,c)[39]. A photocatalytic hydrogen-evolution CDC reaction between thiophene **8** (synthesized from benzenesulfonyl chloride and thiophene-2-ethylamine) and ethylene glycol was performed at a 50-mmol scale using the HSCF platform, yielding 7.36 g of coupling product **10** (45% yield). The resulting free alcohol **10** was directly oxidized to linotroban using silver oxide[48]. This method offers an improvement over the previously reported eight-step synthetic route for linotroban[48], reducing both the number of steps and overall costs. Another example is the streamlined synthesis of LG 82-4-01, a thromboxane (TX) synthetase inhibitor[8], which traditionally requires an eight-step synthesis involving multiple protection and deprotection steps[49]. By utilizing 4-chloro-2-methylthiophene and ethylene glycol as starting materials, the C(sp^2)–O bond coupling product **13** was achieved with a 64% yield using the HSCF platform. A subsequent Mitsunobu reaction using 1*H*-imidazole as the nucleophile, followed by oxidation with $KMnO_4$, delivered LG 82-4-01 in a three-step process from a simple thiophene substrate. Furthermore, the C(sp^2)–N coupling was successfully applied to synthesize melatonin derivative **18**, which exhibited pronounced antioxidant and protective activities[50]. Using the HSCF platform, compound **17** was efficiently synthesized with 65% yield on a decagram scale, and then underwent a deprotection process to yield the target melanin derivative **18** in good yield. These examples of streamlined synthesis of pharmaceutical molecules exemplify the efficacy and practicality of our SAPC-promoted CDC strategy, substantially enhancing the step- and atom-efficiency of pharmaceutical synthesis. Moreover, these examples demonstrate the efficiency and practical utility of the HSCF reactor in scaling up heterogeneous photocatalysis.

Mechanistic elucidation with supporting evidence

To elucidate the reaction mechanism, a series of control experiments were conducted (Fig. 7a). First, no reaction occurred in the presence of radical scavengers, such as (2,2,6,6-tetramethylpiperidin-1-yl)oxyl (TEMPO) or 5,5-dimethyl-1-pyrroline *N*-oxide (DMPO), supporting a radical-involved transformation, while the successful detection of radical-TEMPO adduct indicates the formation of a radical intermediate after the nucleophilic attack from alcohol (Supplementary Fig. 9). The addition of the electron scavenger $NaIO_3$ resulted in only a slight decrease in the yield of **3p**. In contrast, the hole scavenger triethanolamine (TEOA) completely suppressed the reaction. These findings indicate that photogenerated holes play a critical role in the formation of cross-coupling products. In the substrate scope investigations, the enhanced scope of (hetero)arenes in C(sp^2)–N bond formation and the distinct regioselectivity observed for 1-methylindazole in C(sp^2)–O and C(sp^2)–N coupling prompted further exploration. Intermolecular competition experiments with alcohol **2b** and 4-chloro-pyrazole **2s** as nucleophiles consistently demonstrated a preference for C(sp^2)–N bond formation over C(sp^2)–O bond formation when both nucleophiles were present. The regioselectivity with 1-methylindazole also corroborated the findings of the substrate scope study, as shown by product **3z** and **4ag** (Fig. 7b). These results suggest that the nucleophilic attack rate of pyrazole substrates (k_N) was higher than that of alcohols (k_{OH}). Additionally, critical insights were obtained from CV measurements of various representative (hetero)arenes (Fig. 7c). While all substrates exhibited oxidation peaks within the catalyst's oxidation range, certain substrates, such as benzothiophene, exclusively reacted in C(sp^2)–N couplings but remained unreactive with alcohols. This observation suggests that the rate of back-electron transfer (BET) for the (hetero)aryl radical cation falls between k_N and k_{OH} (that is, $k_N > k_{BET} > k_{OH}$), implying that the limited scope of (hetero)arenes for C(sp^2)–O coupling could be attributed to the competing BET processes. In the case of 1-methylindazole, two oxidation peaks ($E_{1p/2}$ = 1.71 V, $E_{2p/2}$ = 1.77 V versus Ag/AgCl) were detected, indicating the possibility of double single-electron oxidations of 1-methylindazole to an iminium cation intermediate. This observation suggests that the rate of iminium cation formation could be comparable to the rate of nucleophilic attack by alcohols, thus explaining the distinct regioselectivity observed in the C(sp^2)–O coupling reaction where alkoxylation occurred on the C(sp^3)–H atom of such substrate. In contrast, pyrazole, with higher nucleophilicity, predominantly underwent aryl amination before it can undergo the second single-electron oxidation (Fig. 7b).

Next, a crucial mechanistic question to address is how the further oxidation of the coupling product was prevented, considering its greater tendency to undergo single-electron oxidation due to its more electron-rich nature than the starting (hetero)arene. It is worth noting that exposure of the coupling product **3a** to *n*-hexanol under the standard reaction conditions resulted in an alkoxyl exchange product **3p** with a yield of 9%. This result suggested that, apart from the widely recognized BET mechanism[51,52], the C(sp^2)–O bond homolysis upon light irradiation could also prevent the further oxidation of product. Further control experiments (Fig. 7d), along with the overlap between the UV–vis absorption spectrum of **3a** and the lamp emission spectrum (Supplementary Fig. 13), verified that this functional group swapping only occurred under light. Furthermore, the capture of thienyl radical by TEMPO (Fig. 7d) also supported the occurrence of C(sp^2)–O bond homolysis upon light irradiation. Although additional mechanistic studies are needed to fully elucidate the mechanism, we suspected that the small amount of alkoxyl exchange product **3p** might arise from a nucleophilic attack by the alcohol to the (hetero)aryl radical through a radical-anion coupling process[53–55]. Light on/off experiments demonstrated the essential role of light (Supplementary Fig. 15). The apparent quantum yield (AQY) for the cross-coupling of thiophene **1a** with *n*-hexanol **2b** was determined to be 1.30% (Supplementary Equation (1)). H/D exchange experiments with 3-bromothiophene and D_2O showed no deuteration of 3-bromothiophene, with the starting material fully recovered, ruling out the involvement of transition-metal-catalysed C(sp^2)–H activation and C(sp^2)–M bond formation (Fig. 7e).

Based on the mechanistic studies and previous literature, a plausible reaction mechanism was proposed as depicted in Fig. 7f. Upon light irradiation, photogenerated electron–hole pairs are formed on the surface of Pt-g-C_3N_4, which has a bandgap of 2.80 eV as determined by Mott–Schottky plots (Supplementary Fig. 3) and UV–vis diffuse reflectance spectroscopy. Subsequently, (hetero)arene **1** undergoes single-electron oxidation to form radical cation intermediate **I**, which is then attacked by alcohols to form radical species **II**, confirmed by radical-trapping experiments (Supplementary Fig. 9), and releases a proton. Intermediate **II** is further oxidized on the Pt-g-C_3N_4 surface to form cationic intermediate **III**, which, following β-H elimination, forms the cross-coupling product **3** and concurrently releases a second proton. The released protons undergo reduction at the platinum single-atom sites, which are regarded as electron reservoirs that substantially enhance the charge separation on the photocatalyst, thereby

facilitating efficient production of H_2 and completing the catalytic cycle. It is important to note that the further oxidation of coupling product **3** is hindered by rapid BET processes and the light-mediated homolysis processes. This mechanistic pathway is also operative for other C(sp^2)–heteroatom and C(sp^2)–C coupling reactions involving 1,3-dicarbonyl compounds. In contrast, the decarboxylative alkylation proceeded through a distinct radical generation pathway, wherein alkyl radicals were formed via single-electron oxidation followed by decarboxylation (Supplementary Fig. 10). This process is probably facilitated by the ionization equilibrium of carboxylic acids and driven by concurrent hydrogen evolution.

Conclusions

We have disclosed that Pt-g-C_3N_4 serves as a highly efficient heterogeneous photocatalyst for hydrogen-evolution CDC reactions between (hetero)arenes and nucleophiles, overcoming the long-standing challenge of requiring stoichiometric oxidants in CDC reactions. Notably, Pt-g-C_3N_4 exhibits remarkable stability, negligible metal leaching and excellent recyclability, while efficiently catalysing reactions across a broad substrate scope even at low catalyst loading. This includes eight classes of (hetero)arenes, namely, thiophenes, furans, pyrroles, indoles, imidazo[1,2-*b*]pyridazines, indazoles, pyridines, and electron-rich benzenes, and seven distinct types of nucleophiles, namely, alcohols, pyrazoles, 1,3-dicarbonyl compounds, carbamates, disulfonimides, carboxylic acids and diarylphosphine oxides. Moreover, the use of HSCF technology for this protocol enables the streamlined synthesis of pharmaceutical molecules on a decagram scale, underscoring the practicality of this method. Our protocol aligns with most of the 12 principles of green chemistry[56], showcasing the remarkable potential of SAPCs in driving hydrogen-evolution CDC reactions and representing a substantial advancement in the field of sustainable chemistry.

Methods

Synthesis of Pt-g-C_3N_4 catalyst

g-C_3N_4 was synthesized by calcining dicyandiamide at 550 °C at a heating rate of 2.3 °C min^{-1} in a crucible for 3 h in static air. This was followed by thermal exfoliation at 500 °C with a heating rate of 5 °C min^{-1} for 5 h in static air. $H_2PtCl_6{\cdot}6H_2O$ (65.0 mg) and g-C_3N_4 (5 g) were dispersed in 500 ml H_2O and sonicated for 2 h, followed by rotary evaporation to dryness. The collected powder was then dried in an oven at 80 °C, followed by heating to 300 °C at a rate of 5 °C min^{-1} for 5 h under a flow of nitrogen. The powder was then thoroughly washed with dimethylsulfoxide and dried again in an oven at 80 °C. Finally, the powders were heated to 500 °C at a rate of 2 °C min^{-1} and maintained for 5 h under nitrogen protection to obtain 4.7 g of Pt-g-C_3N_4.

Materials characterizations

Wide-angle XRD patterns were recorded using a Bruker D8 Focus Powder X-ray diffractometer with copper Kα radiation (40 kV, 40 mA) at room temperature. ICP-OES was measured with an Agilent 720ES with a VistaChip II CCD detector. Transmission electron microscopy images were taken using an FEI Titan 80-300 S/TEM at 200 kV. ADF-STEM images were obtained using an aberration-corrected JEOL ARM-200F system equipped with a cold field emission gun at 60 kV. UV–vis diffuse reflectance spectroscopy was performed on a PerkinElmer Lambda 650 instrument with a detection range of 300–700 nm. XPS measurements were performed in a custom-built ultrahigh-vacuum system with a base pressure below 2×10^{-10} mbar, using aluminium Kα radiation ($h\nu$ = 1486.7 eV) as the excitation source. XANES and EXAFS measurements were performed at the XAFCA beamline of the Singapore Synchrotron Light Source (SSLS), using a Si (111) double-crystal monochromator to filter the X-ray beam. High-resolution XANES used the third harmonic of the Si (111) double-crystal monochromator and the EXAFS oscillations $\chi(k)$ were extracted and analysed using the Demeter software package. Electrochemical measurements were conducted on a CHI660E electrochemical workstation in a standard three-electrode system using a platinum wire as the counterelectrode and saturated Ag/AgCl (3.5 M KCl) as the reference electrode.

General procedure for hydrogen-evolution cross-coupling reactions

A 10-ml Schlenk tube with a magnetic stir bar was charged with Pt-g-C_3N_4 (0.5 wt.%, 16.3 mg), (hetero)arenes (0.5 mmol), nucleophiles (1.5 mmol, 3 equiv.), $Zn(OTf)_2$ (10 mol%, 18.2 mg) and MeCN (0.5 ml) under argon atmosphere. Then, the reaction tube was exposed to a 40-W light-emitting diode (LED) light (370 nm) at room temperature for 24 h. After that, the reaction mixture was removed from the light source and diluted with 3 ml of CH_2Cl_2. The mixture was filtered and washed with 10–20 ml of CH_2Cl_2. The filtrate was concentrated and the residue was purified by column chromatography over silica gel or by preparative thin-layer chromatography to give the corresponding products.

Recycling test

A 10-ml Schlenk tube with a magnetic stir bar was charged with Pt-g-C_3N_4 (0.5 wt.%, 16.3 mg), 3-bromothiophene **1b** (0.5 mmol, 47 µl), *n*-hexanol **2b** (1.5 mmol, 3 equiv., 188 µl), $Zn(OTf)_2$ (10 mol%, 18.2 mg) and MeCN (0.5 ml) under an argon atmosphere. Then, the reaction tube was exposed to a 40-W LED light (370 nm) at room temperature for 24 h. After that, the reaction mixture was removed from the light source and diluted with 3 ml of CH_2Cl_2. The mixture was filtered and washed with 10–20 ml of CH_2Cl_2. The filtrate was concentrated and the residue was purified by column chromatography over silica gel (*n*-hexane) to give product **3b**. The catalyst was washed with 1,4-dioxane, ethanol and deionized water three times, and dried at 80 °C for 12 h before the next reaction cycle.

High-speed circulation flow synthesis

A 100-ml Duran screw-cap bottle was charged with MeCN (50 ml), $Zn(OTf)_2$ (10 mol%, 1.82 g), Pt-g-C_3N_4 (0.50 wt%, 0.04 mol%, 815 mg), the (hetero)arene (50 mmol) and nucleophile (150 mmol, 3 equiv.) successively. The resulting suspension was degassed via argon sparging for 30 min under vigorous stirring, followed by ultrasonication for 10 min. After pretreatment, the flow reactor tubing system was purged with argon for 20 min. Subsequently, the tubing was connected to the Duran bottle under argon. The peristaltic pump was started at a fixed flow rate of 300 ml min^{-1}. Upon complete filling of the tubing system (tubing volume, 50 ml) with the reaction mixture, the air cooling was engaged. With appropriate eye protection implemented, irradiation was commenced using three parallel LED arrays (LED lights: 3 sets, 40 W per set, λ = 370 nm; solvent volume, 60 ml). The photochemical reaction was allowed to proceed for 48 h, after which all irradiation and cooling systems were deactivated. The crude reaction mixture was transferred into a 250-ml round-bottom flask, with thorough rinsing using 100 ml dichloromethane. The combined crude mixture was subjected to centrifugation (4,500 r.p.m., 10 min, relative centrifugal force, 1,920*g*). The supernatant was collected and concentrated under reduced pressure. The resulting residue was purified by column chromatography over silica gel to provide the desired product.

Data availability

Data supporting the findings of this study are available within the paper and its Supplementary Information or from the authors upon request. Source data are provided with this paper.

References

1. Kosman, M. E. Timolol in the treatment of open angle glaucoma. *JAMA* **241**, 2301–2303 (1979).
2. Kjekshus, J. K. et al. Effect of piboserod, a 5-HT_4 serotonin receptor antagonist, on left ventricular function in patients with symptomatic heart failure. *Eur. J. Heart Fail.* **11**, 771–778 (2009).

3. Van Weelderen, M. W.-B. & Van Mullem, P. J. Histological investigation of the effect of a controlled-released anti-inflammatory drug on exposed inflamed dog pulps. *Biomaterials* **4**, 165–169 (1983).
4. Zhang, Y. et al. Dissipation dynamics and dietary risk assessment of pyraclonil residues in rice (*Oryza sativa* L.). *Microchem. J.* **152**, 104440 (2020).
5. Huber, K., Yasothan, U., Hamad, B. & Kirkpatrick, P. Prasugrel. *Nat. Rev. Drug Discov.* **8**, 449–450 (2009).
6. Feng, Y., Park, H., Bauer, L., Ryu, J. C. & Yoon, S. O. Thiophene-pyrazolourea derivatives as potent, orally bioavailable, and isoform-selective JNK3 inhibitors. *ACS Med. Chem. Lett.* **12**, 24–29 (2021).
7. Dorner, G. T. et al. Cisplatin-induced renal effects and thromboxane A_2 receptor blockade. *Eur. J. Clin. Invest.* **27**, 836–839 (1997).
8. Smith III, E. F., Darius, H., Ferber, H. & Schrör, K. Inhibition of thromboxane and 12-HPETE formation by dazoxiben and its two thiophenic acid-substituted derivatives. *Eur. J. Pharmacol.* **112**, 161–169 (1985).
9. Yang, Q., Zhao, Y. & Ma, D. Cu-mediated Ullmann-type cross-coupling and industrial applications in route design, process development, and scale-up of pharmaceutical and agrochemical processes. *Org. Process Res. Dev.* **26**, 1690–1750 (2022).
10. Ruiz-Castillo, P. & Buchwald, S. L. Applications of palladium-catalyzed C–N cross-coupling reactions. *Chem. Rev.* **116**, 12564–12649 (2016).
11. Miyaura, N. & Buchwald, S. L. *Cross-coupling Reactions: A Practical Guide* Vol. 219 (Springer, 2002).
12. Enthaler, S. & Company, A. Palladium-catalysed hydroxylation and alkoxylation. *Chem. Soc. Rev.* **40**, 4912–4924 (2011).
13. Bhadra, S., Matheis, C., Katayev, D. & Gooßen, L. J. Copper-catalyzed dehydrogenative coupling of arenes with alcohols. *Angew. Chem. Int. Ed.* **52**, 9279–9283 (2013).
14. Bras, J. L. & Muzart, J. Dehydrogenative (hetero)arene alkoxylations triggered by Pd^{II} catalyzed C(sp^2)–H activation and coordinating substituent: $Pd^{II,III}$ or Pd^{IV} complex as key intermediate? *Eur. J. Org. Chem.* **2017**, 3528–3548 (2017).
15. Chen, J.-H. et al. Cobalt/salox-catalyzed enantioselective dehydrogenative C–H alkoxylation and amination. *Angew. Chem. Int. Ed.* **61**, e202210106 (2022).
16. Park, Y., Kim, Y. & Chang, S. Transition metal-catalyzed C–H amination: scope, mechanism, and applications. *Chem. Rev.* **117**, 9247–9301 (2017).
17. Kim, H., Heo, J., Kim, J., Baik, M.-H. & Chang, S. Copper-mediated amination of aryl C–H bonds with the direct use of aqueous ammonia via a disproportionation pathway. *J. Am. Chem. Soc.* **140**, 14350–14356 (2018).
18. Zheng, Y.-W. et al. Photocatalytic hydrogen-evolution cross-couplings: benzene C–H amination and hydroxylation. *J. Am. Chem. Soc.* **138**, 10080–110083 (2016).
19. Sun, M. et al. Controllable chemoselectivity in the reaction of 2*H*-indazoles with alcohols under visible light irradiation: synthesis of C3-alkoxylated 2*H*-indazoles and *ortho*-alkoxycarbonylated azobenzenes. *Org. Chem. Front.* **8**, 4230–4236 (2021).
20. Romero, N. A., Margrey, K. A., Tay, N. E. & Nicewicz, D. A. Site-selective arene C–H amination via photoredox catalysis. *Science* **349**, 1326–1330 (2015).
21. Margrey, K. A., McManus, J. B., Bonazzi, S., Zecri, F. & Nicewicz, D. A. Predictive model for site-selective aryl and heteroaryl C–H functionalization via organic photoredox catalysis. *J. Am. Chem. Soc.* **139**, 11288–111299 (2017).
22. Niu, L. et al. Photo-induced oxidant-free oxidative C–H/N–H cross-coupling between arenes and azoles. *Nat. Commun.* **8**, 14226 (2017).
23. Yu, J.-X., Cheng, Y.-Y., Chen, B., Tung, C.-H. & Wu, L.-Z. Cobaloxime photocatalysis for the synthesis of phosphorylated heteroaromatics. *Angew. Chem. Int. Ed.* **61**, e202209293 (2022).
24. Zhang, L. et al. Photoelectrocatalytic arene C–H amination. *Nat. Catal.* **2**, 366–373 (2019).
25. Sauermann, N., Meyer, T. H., Tian, C. & Ackermann, L. Electrochemical cobalt-catalyzed C–H oxygenation at room temperature. *J. Am. Chem. Soc.* **139**, 18452–118455 (2017).
26. Zhou, G. et al. Base-promoted electrochemical Co^{II}-catalyzed enantioselective C–H oxygenation. *Angew. Chem. Int. Ed.* **62**, e202302964 (2023).
27. Yang, Q.-L. et al. Copper-catalyzed electrochemical C–H amination of arenes with secondary amines. *J. Am. Chem. Soc.* **140**, 11487–111494 (2018).
28. Wu, S. et al. Hole-mediated photoredox catalysis: tris(*p*-substituted)biarylaminium radical cations as tunable, precomplexing and potent photooxidants. *Org. Chem. Front.* **8**, 1132–1142 (2021).
29. Hou, Z.-W., Yan, H., Song, J. & Xu, H.-C. Photoelectrocatalytic C–H amination of arenes. *Green. Chem.* **25**, 7959–7962 (2023).
30. Lai, X.-L., Shu, X.-M., Song, J. & Xu, H.-C. Electrophotocatalytic decarboxylative C–H functionalization of heteroarenes. *Angew. Chem. Int. Ed.* **59**, 10626–10632 (2020).
31. Wang, S., Xue, Q., Guan, Z., Ye, Y. & Lei, A. Mn-catalyzed electrooxidative undirected C–H/P–H cross-coupling between aromatics and diphenyl phosphine oxides. *ACS Catal.* **11**, 4295–4300 (2021).
32. Yuan, Y. & Lei, A. Is electrosynthesis always green and advantageous compared to traditional methods? *Nat. Commun.* **11**, 802 (2020).
33. Qiao, B. et al. Single-atom catalysis of CO oxidation using Pt_1/FeO_x. *Nat. Chem.* **3**, 634–641 (2011).
34. Xue, Z.-H., Luan, D., Zhang, H. & Lou, X. W. D. Single-atom catalysts for photocatalytic energy conversion. *Joule* **6**, 92–133 (2022).
35. Li, H., Li, R., Liu, G., Zhai, M. & Yu, J. Noble-metal-free single- and dual-atom catalysts for artificial photosynthesis. *Adv. Mater.* **36**, 2301307 (2024).
36. Vijeta, A., Casadevall, C., Roy, S. & Reisner, E. Visible-light promoted C–O bond formation with an integrated carbon nitride–nickel heterogeneous photocatalyst. *Angew. Chem. Int. Ed.* **60**, 8494–8499 (2021).
37. Kwak, M. et al. Ni single atoms on carbon nitride for visible-light promoted full heterogeneous dual catalysis. *Chem. Sci.* **13**, 8536–8542 (2022).
38. Bajada, M. A. et al. Light-driven C–O coupling of carboxylic acids and alkyl halides over a Ni single-atom catalyst. *Nat. Synth.* **2**, 1092–1103 (2023).
39. Liu, C. et al. High-speed circulation flow platform facilitating practical large-scale heterogeneous photocatalysis. *Org. Process Res. Dev.* https://doi.org/10.1021/acs.oprd.3c00515 (2024).
40. Rocha, G. F. S. R. et al. Carbon nitride based materials: more than just a support for single-atom catalysis. *Chem. Soc. Rev.* **52**, 4878–4932 (2023).
41. Liu, Q. et al. Vacancy engineered polymeric carbon nitride nanosheets for enhanced photoredox catalytic efficiency. *Cell Rep. Phys. Sci.* **2**, 100491 (2021).
42. Suja, P. et al. Graphitic carbon nitride ($g\text{-}C_3N_4$) based heterogeneous single atom catalysts: synthesis, characterisation and catalytic applications. *J. Mater. Chem. A* **11**, 8599–8646 (2023).

43. Yang, J., Wang, D., Han, H. & Li, C. Roles of cocatalysts in photocatalysis and photoelectrocatalysis. *Acc. Chem. Res.* **46**, 1900–1909 (2013).
44. Wolff, C. M. et al. All-in-one visible-light-driven water splitting by combining nanoparticulate and molecular co-catalysts on CdS nanorods. *Nat. Energy* **3**, 862–869 (2018).
45. Hai, X. et al. Scalable two-step annealing method for preparing ultra-high-density single-atom catalyst libraries. *Nat. Nanotechnol.* **17**, 174–181 (2022).
46. Chen, X. et al. Synthesis, characterization, and structures of a persistent aniline radical cation. *Angew. Chem. Int. Ed.* **51**, 11878–11881 (2012).
47. Shida, N., Imada, Y., Nagahara, S., Okada, Y. & Chiba, K. Interplay of arene radical cations with anions and fluorinated alcohols in hole catalysis. *Commun. Chem.* **2**, 24 (2019).
48. Binder, D., Rovenszky, F. & Ferber, H. P. Thienyloxyacetic acid derivatives, a process for their preparation, and pharmaceutical compositions containing them. European patent no. EP0284892A1 (1988); https://worldwide.espacenet.com/patent/search/family/003500502/publication/EP0284892A1?q=EP0284892A1
49. Binder, D., Pyerin, M. & Pusterer, F. Synthesis of substituted alkoxythiophenes: thiophene analogues of dazoxiben. *Monatsh. Chem.* **130**, 645–651 (1999).
50. Ahmed, H. H., Mannaa, F., Elmegeed, G. A. & Doss, S. H. Cardioprotective activity of melatonin and its novel synthesized derivatives on doxorubicin-induced cardiotoxicity. *Bioorg. Med. Chem.* **13**, 1847–1857 (2005).
51. Ohkubo, K., Kobayashi, T. & Fukuzumi, S. Direct oxygenation of benzene to phenol using quinolinium ions as homogeneous photocatalysts. *Angew. Chem. Int. Ed.* **50**, 8652–8655 (2011).
52. Ohkubo, K., Fujimoto, A. & Fukuzumi, S. Visible-light-induced oxygenation of benzene by the triplet excited state of 2,3-dichloro-5,6-dicyano-*p*-benzoquinone. *J. Am. Chem. Soc.* **135**, 5368–5371 (2013).
53. Marquet, J., Jiang, Z., Gallardo, I., Batlle, A. & Cayón, E. Reductively activated "polar" nucleophilic aromatic substitution of pentafluoronitrobenzene. The $S_{RN}2$ hypothesis revisited. *Tetrahedron Lett.* **34**, 2801–2804 (1993).
54. Rossi, R. A., Pierini, A. B. & Peñéñory, A. B. Nucleophilic substitution reactions by electron transfer. *Chem. Rev.* **103**, 71–167 (2003).
55. Greener, A. J. et al. Radical–anion coupling through reagent design: hydroxylation of aryl halides. *Chem. Sci.* **12**, 14641–14646 (2021).
56. Anastas, P. T., Warner, J. C. *Green Chemistry: Theory and Practice* 30 (Oxford Univ. Press, 1998).

Acknowledgements

Jie Wu and J.L. acknowledge financial support from the Prime Minister's Office of Singapore under its NRF-CRP Programme (NRF-CRP29-2022-0004), the Agency for Science, Technology and Research (A*STAR) under its MTC IRG Grant (Project M22K2c0082), the National Natural Science Foundation of China (22371200) and the NUS (Suzhou) Research Institute. Jie Wu acknowledges financial support from Pfizer (A-8002093-00-00).

Author contributions

Jie Wu conceived and designed the programme. Y.S., X.H., H.D. and L.C. performed materials synthesis and characterization. Y.S. designed and performed the experiments. H.D. and X.Y. helped with the substrate scope. Jiale Wu performed the high-speed circulation flow synthesis. J.C. and G.W. contributed to the data analysis. J.L. and Jie Wu supervised the project progress. Y.S., X.H., H.T.A., J.L. and Jie Wu wrote the paper. All authors discussed and commented on the final paper and contributed to the analysis and interpretation of the results.

Competing interests

The authors declare no competing interests.

Additional information

Supplementary information The online version contains supplementary material available at https://doi.org/10.1038/s41929-025-01450-2.

Correspondence and requests for materials should be addressed to Jiong Lu or Jie Wu.

Peer review information *Nature Catalysis* thanks Tsz Woon Lo and the other, anonymous, reviewer(s) for their contribution to the peer review of this work.

Reprints and permissions information is available at www.nature.com/reprints.

Publisher's note Springer Nature remains neutral with regard to jurisdictional claims in published maps and institutional affiliations.

[1]Department of Chemistry, National University of Singapore, Singapore, Singapore. [2]School of Materials Science and Engineering, Peking University, Beijing, People's Republic of China. [3]School of Chemistry and Materials Science, Jiangsu Key Laboratory of New Power Batteries, Jiangsu Collaborative Innovation Centre of Biomedical Functional Materials, Nanjing Normal University, Nanjing, People's Republic of China. [4]Joint School of National University of Singapore and Tianjin University, Fuzhou, People's Republic of China. [5]National University of Singapore (Suzhou) Research Institute, Suzhou, People's Republic of China. [6]These authors contributed equally: Yang Shi, Xiao Hai, Lei Cheng. ✉e-mail: chmluj@nus.edu.sg; chmjie@nus.edu.sg